Chemical Science

ROYAL SOCIETY OF CHEMISTRY

EDGE ARTICLE

View Article Online
View Journal | View Issue

Cite this: *Chem. Sci.*, 2024, **15**, 16536

All publication charges for this article have been paid for by the Royal Society of Chemistry

Optical activity levels of metal centers controlling multi-mode emissions in low-dimensional hybrid metal halides for anti-counterfeiting and information encryption†

Qiqiong Ren,[a] Guojun Zhou, *[a] Yilin Mao,[a] Nan Zhang,[a] Jian Zhang [a] and Xian-Ming Zhang *[ab]

In-depth insight into the electronic competition principles between inorganic units and organic ligands proves to be extremely challenging for controlling multi-mode emissions in low-dimensional hybrid metal halides (LHMHs). Herein, an efficient blue emission from organic ligand was engineered in $(DppyH)_2MCl_4$ (Dppy = diphenyl-2-pyridylphosphine, M = Zn^{2+}, Cd^{2+}) due to the reverse type I band alignment constructed by optically inert units with nd^{10} shell electrons. By contrast, the optically active $[MnCl_4]^{2-}$ with semi-fully filled $3d^5$ shell electrons prompts the band alignment of type II, resulting in the narrowband green emission of Mn^{2+}, along with an energy transfer from $DppyH^+$ to $[MnCl_4]^{2-}$. Beyond that, the band alignment of $(DppyH)SbCl_4$ is further reversed to type I due to the strong stereochemical activity of $5s^2$ lone-pair electrons, resulting in the triplet-state ($^3P_1 \rightarrow {}^1S_0$) self-trapped exciton (STE) emission of $[SbCl_4]^-$. The conclusion is that the electronic configurations of metal centers govern the optical activity levels of inorganic units, which in turn controls the multi-mode emissions by maneuvering the band alignments. This research provides an enlightening perspective on the multi-mode emissions with tunable photoluminescence and resulting electronic transitions of LHMHs, whose derived emitters can be employed in anti-counterfeiting and information encryption.

Received 29th July 2024
Accepted 13th September 2024

DOI: 10.1039/d4sc05041j

rsc.li/chemical-science

Introduction

Low-dimensional hybrid metal halides (LHMHs) are promising to be an industrialized platform of optical-functional materials in the fields of light-emitting diodes (LEDs)[1–4] and anti-counterfeiting.[5–8] This boom is supported by their multi-mode luminescent behaviors, *i.e.*, free exciton (FE) emission,[9–11] self-trapped exciton (STE) emission,[12–15] and metal ion (*e.g.*, transition metal ions Mn^{2+}, Cr^{3+} or rare-earth ions Eu^{3+}, Tb^{3+}, *etc.*) transition emission,[16–19] as well as organic ligand emission.[20–22] Their resulting electronic transitions strongly depend on the band alignments of LHMHs. As shown in Scheme 1, the band alignment of type I consist of the conduction band minimum (CBM) states of metal cations and the valence band maximum (VBM) states of halogen ions. The highest occupied molecular orbital (HOMO) of organic cations is inferior to the VBM, while the lowest unoccupied molecular orbital (LUMO) of organic cations is superior to the CBM so that the excitons are confined to inorganic fragments and the potential ligand emission is quenched.[23–25] Type II with a band-edge of LUMO–VBM or CBM–HOMO shows relatively complex photoluminescence (PL) behaviours, involving synergistic emissions as well as charge transfer between organic and inorganic components.[26–28] In contrast, the band alignment of reverse type I (HOMO–LUMO)

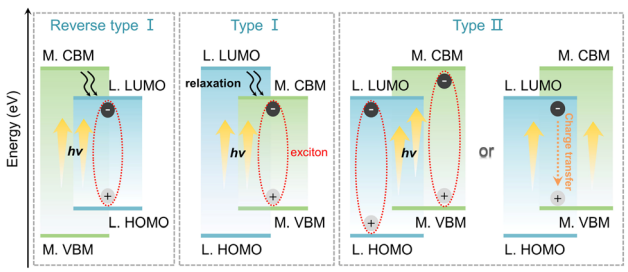

Scheme 1 Three types of band alignments in LHMHs (L and M refer to ligands and metals, respectively). Type I (M. CBM–VBM edged), type II (L. LUMO–M. VBM/M. CBM–L. HOMO edged), and reverse type I (L. LUMO–HOMO edged).

[a]*Key Laboratory of Magnetic Molecules and Magnetic Information Materials (Ministry of Education), School of Chemistry and Material Science, Shanxi Normal University, Taiyuan 030031, P. R. China. E-mail: zhangxm@dns.sxnu.edu.cn*

[b]*College of Chemistry & Chemical Engineering, Key Laboratory of Interface Science and Engineering in Advanced Material, Taiyuan University of Technology, Taiyuan, Shanxi 030024, P. R. China*

† Electronic supplementary information (ESI) available: Details of methods and additional figures and tables. CCDC 2321320–2321324. For ESI and crystallographic data in CIF or other electronic format see DOI: https://doi.org/10.1039/d4sc05041j

allows the excitons to be localized on the organic fragment, thereby facilitating the emission dominated by high-energy excited states of ligands.[29,30] Although the research on the luminescent properties of LHMHs has achieved periodical progress, there is still limited exploration of the competitive emissions between inorganic units and organic ligands along with the resulting electron transition principles.

Aliphatic organic cations with wide bandgaps normally act as charge balancers and isolate inorganic units in LHMHs, without contributing to the band-edges, tending to construct the band alignment of type I.[31–33] Conversely, the electronic states of narrow bandgap organic cations with conjugated configurations can extend to the band-edges and form different band alignments. Lü's group has achieved the above three types of band alignments and the conversion between organic and inorganic emissions by incorporating organic cations with varying conjugation degrees with the $[PbI_4]^{2-}$ inorganic unit. This highlights the crucial role of ligands in the band-edge manipulation and multi-mode emissions of LHMHs.[34] To date, the dominant metal centers include the cations of Pb^{2+}, Sb^{3+}, Bi^{3+} and Te^{4+} with ns^2 electron configuration, the cations of Cu^{+}, Cd^{2+}, Zn^{2+} and In^{3+} with nd^{10} electron configuration, and the cation of Mn^{2+} with $3d^5$ electron configuration.[35] The majority of the reported ns^2-based LHMHs present type I band alignment, with the s orbital of metal cations occupying the VBM and the p orbitals of metal and halogen occupying the CBM, resulting in STE emission from the inorganic units.[36–38] By contrast, the nd^{10}-based LHMHs not only form the type I band alignment composed of the p orbital of halogen as well as s and d orbitals of metal cations but also form type II and reverse type I band alignment involving π and π^* orbitals of organic cations, corresponding to the STE emissions of inorganic units, the organic ligand emissions as well as the synergistic emissions of organic and inorganic components.[20,39,40] Besides, the prevailing Mn^{2+}-based ($3d^5$) LHMHs typically exhibit the d–d transitions ($^4T_1 \rightarrow {}^6A_1$) of Mn^{2+}.[41,42] Neverthless, the working mechanism of metal centers to control multi-mode emissions remains ambiguous, especially when coupled to ligand emission.

Herein, we screened the conjugated aromatic ligand diphenyl-2-pyridylphosphine (Dppy) for assembly with inorganic units $[MCl_4]^{n-}$ (M = Zn^{2+}, Cd^{2+}, Mn^{2+}, and Sb^{3+}) with $3d^{10}$, $4d^{10}$, $3d^5$ and $5s^2$ electronic configurations, respectively. $(DppyH)_2MCl_4$ (M = Zn^{2+} and Cd^{2+}) display an efficient blue emission from the organic ligand, which is attributed to the reverse type I band alignment induced by the large electronegativity and optical inertness of fully-filled nd^{10} shell electrons. However $(DppyH)_2MnCl_4$ with semi-fully filled $3d^5$ shell electrons constructs the band alignment of type II and exhibits the double-peaked emissions from $[MnCl_4]^{2-}$ and $DppyH^+$ at low temperatures. Beyond that, the $5s^2$ lone-pair electrons with stronger stereochemical activity promote $(DppyH)SbCl_4$ to reverse the band alignment of type II to type I, resulting in the broadband orange STE emission of $[SbCl_4]^{-}$. This work highlights the crucial role of the optical activity levels of metal centers in controlling the band alignments and multi-mode emissions while revealing the electronic competition principles between inorganic units and organic ligands. Accordingly, the derivative emitters with abundant light-colors are employed in anti-counterfeiting and information encryption.

Experimental section

Materials

The raw materials diphenyl-2-pyridylphosphine ($C_{17}H_{14}NP$, 98%, Energy Chemical), zinc chloride ($ZnCl_2$, 98%, Aladdin), cadmium chloride hemi(pentahydrate) ($CdCl_2 \cdot 2.5H_2O$, 98%, Aladdin), manganese chloride ($MnCl_2$, ≥99%, Aladdin), antimony trichloride ($SbCl_3$, 99%, Macklin), hydrochloric acid (HCl, 37%, Aladdin) and ethanol (C_2H_5OH, 99.7%, Guangfu) were used without any further purification.

Preparation of single crystals

Growth of $(DppyH)_2ZnCl_4$ single crystals. Dppy (1 mmol, 0.2633 g) was dissolved in 1.5 mL HCl for protonation. After stirring for 10 min, $ZnCl_2$ (0.5 mmol, 0.0682 g) and 3 mL EtOH were added to the above solution as well as heated and stirred at 70 °C to form a clear solution. Then the container was covered and sealed, and the hydrothermal reactor was placed in an oven at 80 °C. The high-quality single crystals were obtained by decreasing the temperature to 25 °C at a rate of 0.5 °C per hour. The synthetic procedures for $(DppyH)_2CdCl_4$, $(DppyH)_2MnCl_4$ and $(DppyH)SbCl_4$ are similar to that for $(DppyH)_2ZnCl_4$.

Characterization

Single-crystal X-ray diffraction (SCXRD) data of Dppy and $(DppyH)_2CdCl_4$ were collected at 293(2) K using an XtaLAB AFC12 X-ray four-circle single crystal diffractometer (Rigaku) equipped with a CCD-detector, graphite monochromator and Mo-Kα radiation source. The SCXRD data of $(DppyH)_2ZnCl_4$, $(DppyH)_2MnCl_4$ and $(DppyH)SbCl_4$ were collected using a D8 Venture diffractometer (Bruker) with Mo-Kα radiation (λ = 0.71073 Å). Hirshfeld surfaces and the corresponding 2D fingerprint plots of $[MX_4]^{2-}$ metal halide anions were calculated using the Crystal Explorer 21.5 program.[43,44] Powder X-ray diffraction (PXRD) patterns were measured on a Rigaku MiniFlex600 diffractometer with a Cu target tube operating at 40 kV and 15 mA at room temperature (RT) in the 2θ range of 5–50°. The morphology analysis and elemental mappings were conducted on a scanning electron microscope (SEM, JEOL JSM-6510). Fourier transform infrared (FTIR) spectra were obtained using an FTIR-650 spectrometer (frequency range from 4000 to 400 cm^{-1}) with a KBr pellet. The ultraviolet visible absorption spectroscopy (UV-Vis) was performed on a TU-1901 ultraviolet spectrometer at RT and $BaSO_4$ was used as the reflectance standard reference. The PL and photoluminescence excitation (PLE) spectra and photoluminescence quantum yields (PLQYs) were measured using an Edinburgh FLS920 fluorescence spectrometer with a picosecond pulsed diode laser. The temperature-dependent spectra were measured on the Edinburgh FLS980 fluorescence spectrometer equipped with the cryogenic liquid nitrogen plant equipment. PL decay

data were collected at RT using an FLS1000 spectrofluorometer using a microsecond light source.

Computational methods

Density functional theory (DFT) calculations were carried out using the Vienna *ab initio* simulation package code (VASP).[45,46] The Heyd–Scuseria–Ernzerhof (HSE06)[47] was applied to calculate the bandgap and electronic properties. A cutoff energy of 400 eV was used for the plane-wave basis set in structural optimizations and electronic structure calculations. The convergence criterion was the energy difference between two consecutive steps of the calculations less than 10^{-6} eV. Besides, the Gaussian 09 program[48] was used to simulate the HOMO and LUMO distributions.

Results and discussion

Structure design and characterization

The aromatic ligand $DppyH^+$ was employed as an organic cationic template to assemble with inorganic units $[ZnCl_4]^{2-}$, $[CdCl_4]^{2-}$, $[MnCl_4]^{2-}$ and $[SbCl_4]^-$ with distinct optical activity levels, as shown in Fig. 1a. SCXRD data show that both $(DppyH)_2ZnCl_4$ and $(DppyH)_2CdCl_4$ are isostructural, belonging to the congruent monoclinic space group $C2/c$. They display a unique zero-dimensional (0D) isolated structure, in which Zn and Cd atoms are coordinated with four Cl atoms to form individual $[MCl_4]^{2-}$ twisted tetrahedron units. The organic cations $DppyH^+$ separate the inorganic units from each other (Fig. 1b and S1a†), resulting in strong quantum confinement and dielectric confinement effects. The Cd–Cl distances are longer than that of Zn–Cl due to the larger ionic radius of Cd^{2+} than that of Zn^{2+}. $(DppyH)_2MnCl_4$ with a 0D structure also belongs to the monoclinic space group $C2/c$, but the stacking orientation is opposite to that of $(DppyH)_2MCl_4$ ($M = Zn^{2+}$ and Cd^{2+}) (Fig. 1c). By contrast, $(DppyH)SbCl_4$ is unusual in that the Sb atom is coordinated to five Cl atoms to form a $[SbCl_5]^{2-}$ pyramid, which are interconnected by nodes to form an infinitely corrugated one-dimensional (1D) chain along the *b*-axis (Fig. 1d). Among them, the Sb–Cl bond lengths between bridged Cl^- and central Sb^{3+} are 2.940 Å and 3.017 Å respectively, which are regarded as Sb···Cl secondary bonds (>2.90 Å). Therefore, the inorganic anion chain is actually constructed from multiple $[SbCl_3]$ trigonal units and free Cl^- through Sb···Cl secondary bonds.[31] The Hirshfeld d_{norm} surfaces and 2D fingerprint plots point to the intermolecular interactions between organic and inorganic units (Fig. S2–S5†). The crystallographic information files (CIFs) are presented in the ESI,† and the main bond lengths and bond angles are listed in Tables S1–S9.† The FTIR, PXRD and energy dispersive X-ray spectroscopy (EDS) elemental mapping analyses (Fig. S6–S8†) were performed to further verify the phase-purity and associated chemical compositions.

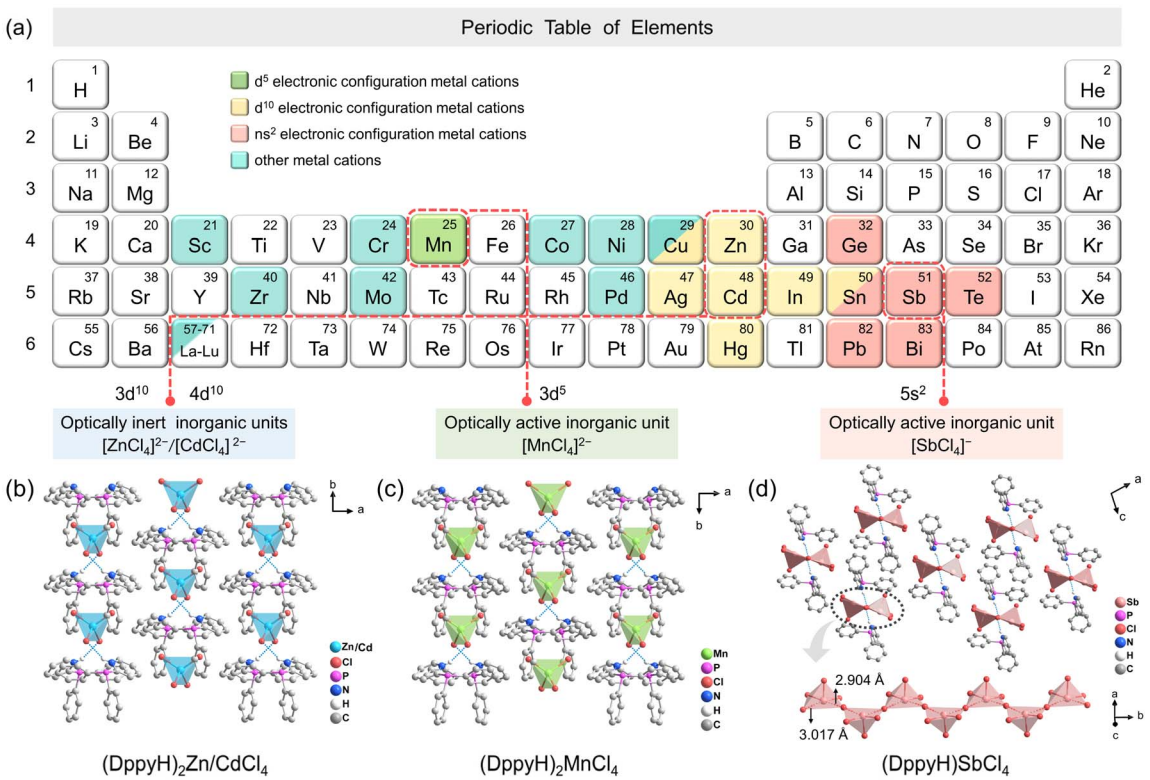

Fig. 1 (a) Periodic table of elements. (b and c) The packing diagrams of the crystal structures of $(DppyH)_2MCl_4$ ($M = Zn^{2+}$, Cd^{2+}, and Mn^{2+}) along the crystallographic *c*-axis. (d) The packing diagram of the crystal structure of $(DppyH)SbCl_4$ along the crystallographic *b*-axis, and 1D inorganic infinite chain composed of corner-sharing $[SbCl_5]^{2-}$ pyramids (the blue dashed lines represent hydrogen bonds and partial hydrogen atoms are omitted).

Optical properties and mechanism investigation

The UV-Vis absorption spectra in Fig. S9† indicate that the organic ligand Dppy possesses two absorption peaks at 262 nm and 318 nm, corresponding to the π → π* and n → π* electronic transitions of the benzene and pyridine rings.[27,28] $(DppyH)_2MCl_4$ (M = Zn^{2+} and Cd^{2+}) show similar peak shapes to Dppy, but their absorption bands are broadened, with the bandgaps of 2.95 eV and 2.93 eV, respectively. $(DppyH)_2MnCl_4$ and $(DppyH)SbCl_4$ show a wider absorption range from ultraviolet to visible light, as well as narrower bandgaps of 2.85 eV and 2.53 eV, respectively. The optical photograph and CIE chromaticity diagrams are illustrated in Fig. S10.† Subsequently, we have thoroughly investigated their PL properties. As shown in Fig. 2a, Dppy displays a weak blue emission at 470 nm with a full width at half maximum (FWHM) of 98 nm under UV excitation. The PLE and PL spectra in $(DppyH)_2MCl_4$ (M = Zn^{2+} and Cd^{2+}) almost overlap with that of Dppy (Fig. 2a). Meanwhile, the PL decay curves show a biexponential decay trend and similar lifetime (Fig. S11†), indicating that the blue emission of $(DppyH)_2MCl_4$ (M = Zn^{2+} and Cd^{2+}) is derived from the singlet-state ($S_1 \rightarrow S_0$) of Dppy. The wavelength-dependent PL and PLE spectra (Fig. S12†) further indicate that the intervention of optically inert units $[ZnCl_4]^{2-}$ and $[CdCl_4]^{2-}$ with d^{10} electronic configuration into the optically active ligand cannot modulate the original electronic transition path.

In addition, the inorganic units of $[MX_4]^{2-}$ (M = Zn^{2+}, Cd^{2+} and X = Cl^-) are discussed as the individual binary discrete system, in which the valence band includes primarily the orbitals of the anion X^-, while the conduction band includes primarily the orbitals of metal cation M^{n+}. The energy gap, E_g, involving electron transfer from the valence band to the conduction band, can be qualitatively estimated from the equation:[49]

$$E_g = 3.72 \times (\chi_{anion} - \chi_{cation}) \quad (1)$$

where χ_{anion} and χ_{cation} refer to the optical electronegativity of the anion and cation, respectively. According to Pauling's electronegativity scale,[50] the electronegativity values of Zn, Cd, and Cl are listed in Fig. 2a. The significant difference in electronegativity between metals and halogen results in a wide bandgap and high conduction band positions in $[ZnCl_4]^{2-}$ and $[CdCl_4]^{2-}$. As a result, the binary system is incorporated into the aromatic conjugated ligand with a narrow bandgap, and the ligand primarily occupies the frontier orbitals. Besides, the fully-filled $nd^{10}(n+1)s^0$ shell electrons exhibit optical inertness. In response to the tetrahedral crystal field, degenerate d orbitals are split into t_{2g} and e_g energy levels, and the outer s orbital is split into a_{1g} energy levels. According to the Pauli exclusion principle, the d–d transition is prohibited, and the transfer of excited electrons from the d orbital energy levels to the s orbital energy level (T_d: $t_{2g} \rightarrow a_{1g}$) requires higher energy, thus preferring the singlet-state ($S_1 \rightarrow S_0$) emission of Dppy. The corresponding electron transitions are depicted in Fig. 2a. Upon incorporation of the optically inert units $[ZnCl_4]^{2-}$ and $[CdCl_4]^{2-}$ into the ligand, the new energy levels are populated in the conduction band of the organic fragment without changing the initial band-edge compositions, causing excited electrons to aggregate at the lowest excitation level of the ligand through non-radiative transitions, thereby facilitating the high-energy emission of Dppy.

Not only that, the introduction of $[MCl_4]^{2-}$ (M = Zn^{2+} and Cd^{2+}) significantly improves the PLQYs (Fig. 2b). The reasons

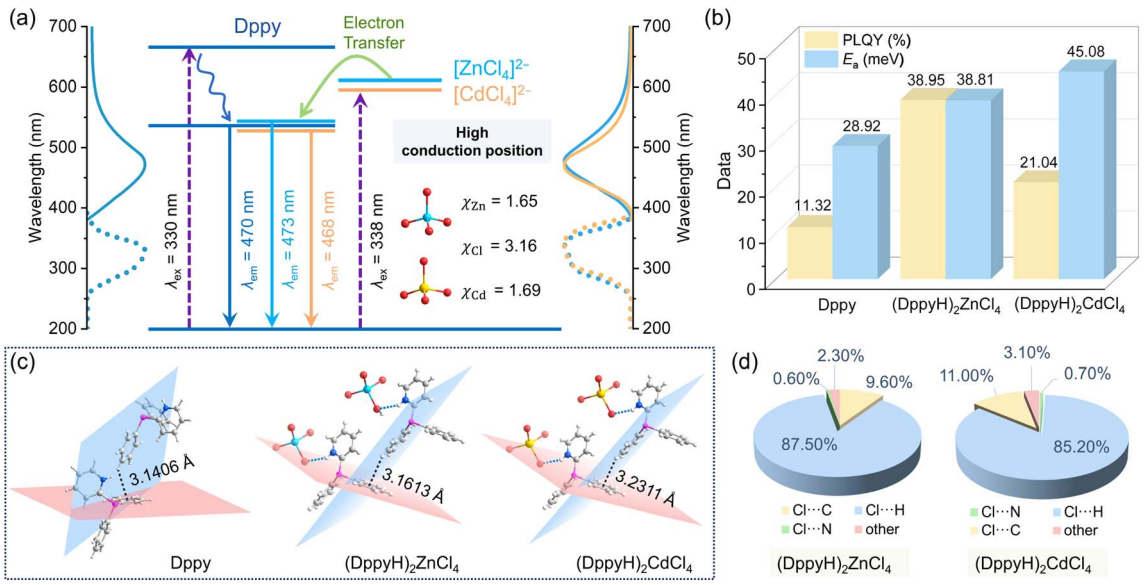

Fig. 2 (a) The PLE and PL spectra of Dppy and $(DppyH)_2MCl_4$ (M = Zn^{2+} and Cd^{2+}) and the corresponding schematic diagram of the luminescence mechanism. (b) PLQYs and the activation energy E_a of Dppy and $(DppyH)_2MCl_4$ (M = Zn^{2+} and Cd^{2+}). (c) The stacking diagrams of C–H···π interaction (black dotted line) between adjacent organic ligands in Dppy and $(DppyH)_2MCl_4$ (M = Zn^{2+} and Cd^{2+}) and the N–H···Cl interaction (blue dotted line) between the organic cation $DppyH^+$ and the inorganic unit $[MCl_4]^{2-}$ (M = Zn^{2+} and Cd^{2+}). (d) Percentage contributions of the various close intermolecular contacts of $(DppyH)_2MCl_4$ (M = Zn^{2+} and Cd^{2+}) to the Hirshfeld surface.

are summarized as follows: (1) the embedding of tetrahedral $[ZnCl_4]^{2-}$ and $[CdCl_4]^{2-}$ leads to a larger spacing between the organic ligands (Fig. 2c), thus restraining the self-absorption in the emission centers. (2) The enhanced structural rigidity of $(DppyH)_2MCl_4$ (M = Zn^{2+} and Cd^{2+}) suppresses the non-radiative energy loss. The additional hydrogen bonds between the organic cation and inorganic units allow for greater structural stability, with each $[MCl_4]^{2-}$ unit connecting with six $DppyH^+$ cations and each organic cation connecting to three inorganic units to form a robust three-dimensional (3D) hydrogen bonding network (Fig. S13 and S14†). Fig. 2d illustrates that the C/N–H···Cl hydrogen bonds play a major role in improving structural rigidity. The temperature-dependent PL spectra and the calculated activation energy E_a (Fig. S15†) suggest a significant reduction of the thermally activated non-radiation process after the intervention of inorganic units $[ZnCl_4]^{2-}$ and $[CdCl_4]^{2-}$, thereby improving the PLQYs.

By contrast, utterly distinct photophysical behaviors were observed in $(DppyH)_2MnCl_4$ and $(DppyH)SbCl_4$. As illustrated in Fig. 3a, the PLE spectra show the ultra-broad excitations from the ultraviolet to blue region. Meanwhile, $(DppyH)_2MnCl_4$ exhibits a bright green emission at 522 nm with a narrow FWHM of 60 nm and a PLQY of 50.82%. The PL decay curve (Fig. S16a†) can be fitted with a single-exponential equation: $I(t) = I_0 + A\exp(-t/\tau)$, with a lifetime of 2.45 ms, which coincides with the reported hybrid Mn^{2+}-based chlorides, demonstrating that the emission belongs to the d–d transition ($^4T_1 \rightarrow {}^6A_1$) of Mn^{2+}.[51,52] The wavelength-dependent PLE/PL spectra (Fig. S17a and b†) indicate the existence of a single electron transition pathway and uniform excited state in $(DppyH)_2MnCl_4$ at RT. The temperature-dependent PL spectra (Fig. 3b) indicate that the PL intensity gradually increases as the temperature decreases, and it is noted that an appended emission peak appears at 463 nm. The PL decay curves at 80 K (Fig. S18†) indicate that the luminescence mechanism at 463 nm is different from the emission at 522 nm from $[MnCl_4]^{2-}$. The nanosecond level lifetime (0.71 ns) is consistent with that of organic ligands. Considering the significant overlap between the PL spectrum of Dppy and the PLE spectrum of $[MnCl_4]^{2-}$ (Fig. 3a), it is speculated that there is an energy transfer from $DppyH^+$ to $[MnCl_4]^{2-}$. Consequently, the emission at 463 nm can be attributed to the organic ligand, in turn, $(DppyH)_2MnCl_4$ exhibits a synergistic emission of $DppyH^+$ and $[MnCl_4]^{2-}$ at low temperatures. $(DppyH)SbCl_4$ exhibits a bright orange emission (PLQY = 37.96%) with a large FWHM of 205 nm and a large Stokes shift of 290 nm, implying that the intervention of optically active unit $[SbCl_4]^-$ can modify or even eliminate the original emission channels. The PL decay data (Fig. S16b†) were characterized as biexponential with an average value of 1.65 ns, which is consistent with the triplet-state STE emission ($^3P_1 \rightarrow {}^1S_0$) of LHMHs (Table S10†). Moreover, the wavelength-dependent PLE/PL spectra indicate that there is only the intrinsic emissions from the active units $[SbCl_4]^-$ (Fig. S17c and d†).

The temperature-dependent spectra of $(DppyH)SbCl_4$ (Fig. S19†) were recorded to further validate the luminescence mechanism. The relationship curves between bandwidth (Γ) and temperature are fitted through the following equation:[53]

$$\Gamma(T) = \Gamma_0 + \Gamma_{phonon}(e^{(E_{LO}/k_BT)} - 1)^{-1} + \Gamma_{inhomo}e^{-E_b/k_BT} \quad (2)$$

where Γ_0 represents the FWHM at 0 K, and Γ_{phonon} and Γ_{inhomo} refer to the relative contributions of electron–phonon coupling and trapped states to peaks broadening, respectively. E_{LO} is the

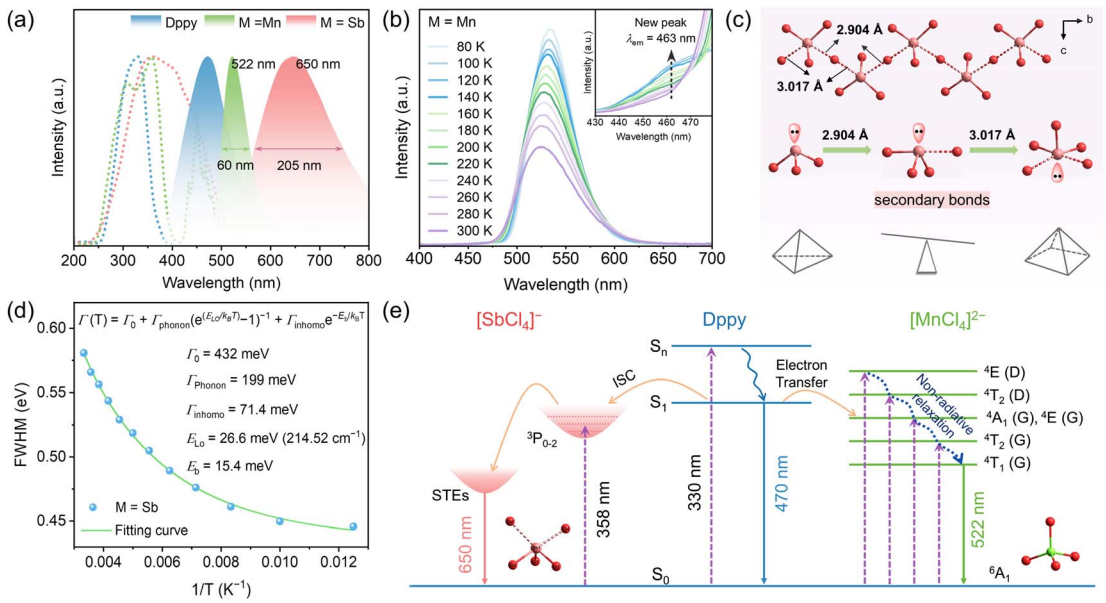

Fig. 3 (a) The PLE and PL spectra of Dppy, $(DppyH)_2MnCl_4$ and $(DppyH)SbCl_4$. (b) Temperature-dependent PL spectra of $(DppyH)_2MnCl_4$. (c) The evolution process of metal halide units (triangle, seesaw, and pyramid) in $(DppyH)SbCl_4$. (d) Bandwidth of the STE emission as a function of 1/T in the range of 80–300 K, in which the green line indicates the fitting data. (e) Schematic diagram of luminescence mechanisms of $(DppyH)_2MnCl_4$ and $(DppyH)SbCl_4$.

energy of the longitudinal optical phonon energy and E_b represents the binding energy of trapped states. The fitting Γ_{phonon} is 199 meV, indicating a strong electron–phonon coupling in $DppyHSbCl_4$ and a larger contribution of electron–phonon coupling to the PL linewidths than the non-uniform broadening effect (Γ_{inhomo}). The calculated phonon value (E_{LO}) is 26.6 meV, which is consistent with the stretching vibration value (215 cm^{-1}) of bridging Sb–Cl bonds, validating that STEs are located at the distorted $[SbCl_5]^{2-}$ pyramid, especially on the bridging Sb–Cl bonds.[54] Also, the Sb···Cl secondary bonds reduce the symmetry of inorganic units, transforming the $[SbCl_3]$ triangle into an extremely twisted $[SbCl_5]^{2-}$ pyramid (Fig. 3c). This amplifies the distortion degree in the geometric structures and provides a soft lattice for the formation of STEs. The bond length distortion (Δd)[55] and bond angle variance (σ^2)[56] were estimated by using formulae (3) and (4), respectively.

$$\Delta d = 1/5 \sum_{i=1}^{5} \left((d_i - d_0)/d_0 \right) \quad (3)$$

where d_0 represents the average Sb–Cl bond length and d_i are five individual lengths of the Sb–Cl bond.

$$\sigma^2 = 1/7 \sum_{i=1}^{8} (\theta_i - 90)^2 \quad (4)$$

where θ_i refers to all Cl–Sb–Cl bond angles. The Δd and σ^2 values of $(DppyH)SbCl_4$ are 1.182×10^{-2} and 26.56, respectively, demonstrating a high distortion degree. Furthermore, the weak interaction between Sb and Cl also contributes to the structural distortion and reorganization of excited states.[57,58]

Accordingly, the PL mechanism of $(DppyH)_2MnCl_4$ and $(DppyH)SbCl_4$ is illustrated in Fig. 3e. In the case of $(DppyH)_2MnCl_4$, all excited electrons move to the lowest excitation level $^4T_1$ of $[MnCl_4]^{2-}$ *via* non-radiative relaxation or energy transfer at RT, and then return to the ground state to generate characteristic emission of Mn^{2+}. The rate of energy transfer from $DppyH^+$ to $[MnCl_4]^{2-}$ is slowed down with decreasing temperature; most excited electrons follow the transition path as at RT to produce green emission, while a few excited electrons directly return from the excited state of the organic cation to the ground state to emit the singlet-state fluorescence ($S_1 \rightarrow S_0$), resulting in the dual emissions of $DppyH^+$ and $[MnCl_4]^{2-}$ at 80 K. For $(DppyH)SbCl_4$, the excited electrons transfer to the triplet-state levels (^3P_n) of $[SbCl_4]^-$ *via* non-radiative relaxation, where the electrons are captured by phonons to form triplet-state STEs, accompanied by the orange emission while quenching the emission of Dppy.

Theoretical calculation

The DFT calculation was conducted to prove the electron transition mechanism. Fig. 4a and S20† show that the regions from −1.8363/−1.9760 eV to 2.0315/1.9834 eV are determined by the p orbital of C, N and P atoms of the organic ligand in $(DppyH)_2ZnCl_4$ and $(DppyH)_2CdCl_4$. They form the band alignment of reverse type I (Fig. 4b), where the orbitals of $DppyH^+$ make the dominant contributions to the VBM states and CBM states, while the orbitals of inorganic units $[ZnCl_4]^{2-}$ and $[CdCl_4]^{2-}$ are away from the band-edges, allowing the optical behaviors to be

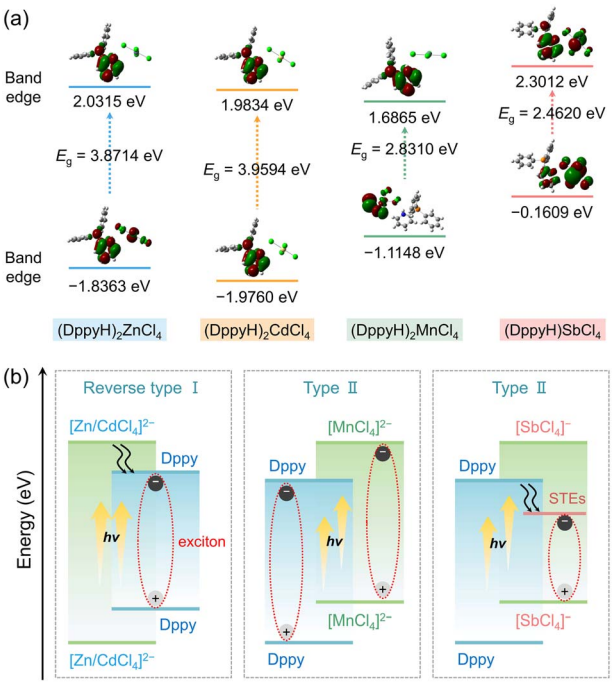

Fig. 4 (a and b) Orbital energy levels and corresponding electronic charge densities for the VBM and CBM as well as band alignments of $(DppyH)_nMCl_4$ (M = Zn^{2+}, Cd^{2+}, Mn^{2+}, and Sb^{3+}).

dominated by the electronic transition of the organic ligand. However, the VBM is dominated by the p orbital of Cl in the inorganic anion $[MnCl_4]^{2-}$, the CBM is occupied by the p orbital of C, N, and P atoms, and the d orbital of Mn appears in the gap of CBM near the band-edge, as for the $(DppyH)_2MnCl_4$, which is aligned with the band alignment of type II. This favors the synergistic emission of $DppyH^+$ and $[MnCl_4]^{2-}$ at low temperatures. In the case of $(DppyH)SbCl_4$, the optically active unit $[SbCl_4]^-$ promotes a narrow bandgap. The VBM is dominated by the s and p orbitals of the Sb atom and the p orbital of the Cl atom, with the p orbital of C and P atoms contributing less to the VBM, whereas the p orbital of C and N atoms as well as the s orbital of the Sb atom dominate the CBM. Although $(DppyH)SbCl_4$ also forms a band alignment of type II, the temporary defect energy levels induced by $5s^2$ lone-pair electrons promote the band alignment change to type I upon excitation, resulting in the excitons strictly localized in the inorganic unit $[SbCl_4]^-$ and producing the STE emission.[59] In addition, the calculated optical bandgaps are 3.8714 eV, 3.9594 eV, 2.8310 eV, and 2.4620 eV for $(DppyH)_nMCl_4$ (M = Zn^{2+}, Cd^{2+}, Mn^{2+}, and Sb^{3+}), respectively (Fig. S21†), which are consistent with the experimental values.

Anti-counterfeiting application

The optical activity levels of metal centers manipulate the band alignments to achieve multi-mode emissions in $(DppyH)_nMCl_4$ (M = Zn^{2+}, Cd^{2+}, Mn^{2+}, and Sb^{3+}), whose tunable fluorescent color-changing behavior provides a prospective approach for information encryption and transmission. A model instrument incorporating the multicolor UV-converted LED devices with cryptographic devices was engineered in this research. Fig. 5a

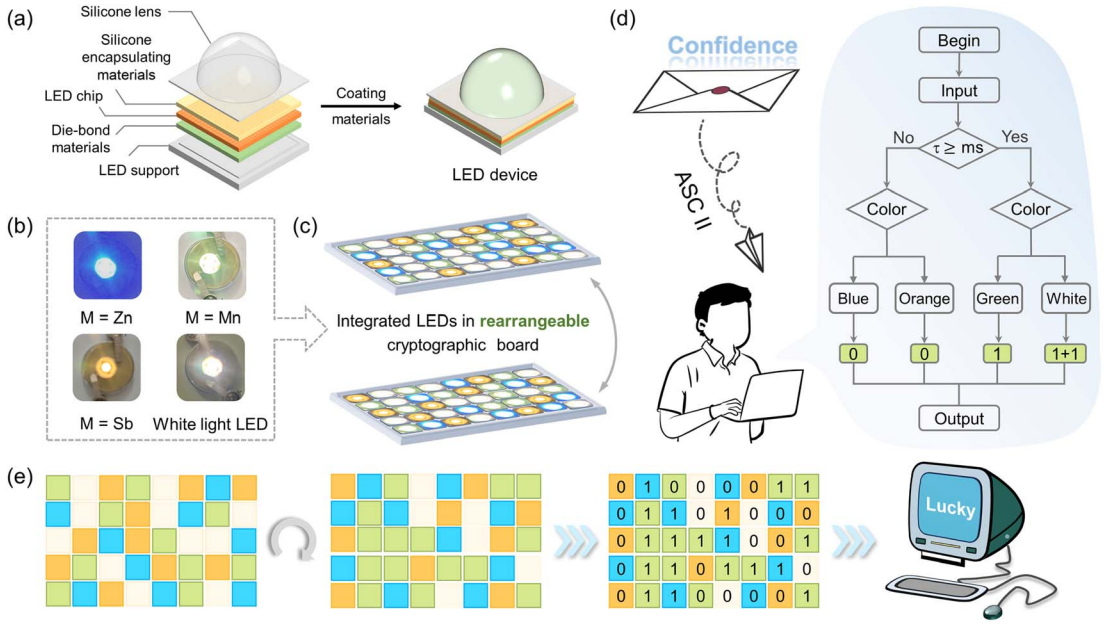

Fig. 5 (a) The internal structure and assembly diagram of LED devices. (b) The physical photographs of blue, green, orange and white LED devices at a current of 20 mA, respectively. (c) The model diagram integrating the above four LEDs in a reconfigurable password board. (d) Logic gate application. (e) LED rearrangement and decoding flowchart.

displays the internal structure and assembly diagram of the LEDs. The blue-emitting $(DppyH)_2ZnCl_4$, green-emitting $(DppyH)_2MnCl_4$, and orange-emitting $(DppyH)SbCl_4$ were coated on the UV InGaN chip (365 nm) to acquire the blue, green, and orange UV-converted LED devices, respectively. The white LED device was encapsulated by mixing the above phosphors in a certain proportion. The physical photographs of the UV-converted LED devices at 20 mA current are presented in Fig. 5b. The model device for information encryption and transmission was achieved by integrating four LED devices with a cryptographic board of 5*8 dots, which shuffles and reassembles the LEDs to facilitate the transmission of information with diverse contents (Fig. 5c). As shown in Fig. 5d, we define such a logic gate based on the differences in PL lifetime and colors excited at 365 nm. To enhance the complexity of data encryption, we reference the addition operation: 1 + 1 = 10 (0 carries 1) of the binary system. The output binary codes can be converted into characters through the American Standard Code for Information Interchange (ASC II) to obtain the encrypted information. Fig. 5e illustrates the realignment process of LED devices and the decoding process for a specific LED arranged cryptographic board, culminating in the output of the word "lucky". The tunable multi-mode emissions in LHMHs are significant for anti-counterfeiting applications.

Conclusions

In summary, novel LHMHs of $(DppyH)_nMCl_4$ ($M = Zn^{2+}$, Cd^{2+}, Mn^{2+}, and Sb^{3+}) were synthesized by incorporating inorganic units with distinct optical activity levels into a highly conjugated organic ligand. $(DppyH)_2MCl_4$ ($M = Zn^{2+}$ and Cd^{2+}) exhibit an efficient blue-light emission from the organic ligand due to the formation of the reverse type I band alignment induced by the optical inertness of fully filled d^{10} shell electrons. The PLQYs are significantly improved due to the weakened self-absorption between organic ligands and enhanced structural rigidity after the intervention of $[MCl_4]^{2-}$ ($M = Zn^{2+}$ and Cd^{2+}). By contrast, the optically active $[MnCl_4]^{2-}$ with semi-full filled $3d^5$ shell electrons constructs the band alignment of type II, resulting in the narrowband green emission from the d–d transition ($^4T_1 \rightarrow {}^6A_1$) of Mn^{2+} in $(DppyH)_2MnCl_4$ at RT. $(DppyH)SbCl_4$ forms an infinite 1D structure connected by Sb···Cl secondary bonds under the strong stereochemical activity of $5s^2$ lone-pair electrons, and the resulting transient defect reverses the band alignment from type II to type I, leading to a bright broadband orange emission from triplet-state ($^3P_1 \rightarrow {}^1S_0$) STEs of $[SbCl_4]^-$. The differences in band alignments engineered by optical activity levels of metal centers further reveal the competition mechanism between organic ligands and inorganic units. The derivative emitters with different light-colors present enormous application prospects in the field of anti-counterfeiting and information encryption.

Data availability

Detailed crystallographic information and supplementary figures and tables can be found in the ESI.† Crystallographic data are available *via* the Cambridge Crystallographic Data Centre (CCDC): 2321320–2321324. The data supporting this article have been included as part of the ESI.†

Author contributions

Qiqiong Ren: prepared and characterised all compounds, conceptualization, investigation, formal analysis, visualization,

writing – original draft; Yilin Mao: investigation, formal analysis; Nan Zhang and Jian Zhang: theoretical calculation; Guojun Zhou and Xian-Ming Zhang: conceptualization, project administration, funding acquisition, supervision, writing – review & editing.

Conflicts of interest

There are no conflicts to declare.

Acknowledgements

Thanks for the invitation for submission to celebrate the 100th anniversary of Sun Yat-sen University. This work was supported by the National Natural Science Foundation of China (No. 52202177), Natural Science Foundation of Shanxi Province (No. 20210302124054), and Shanxi-Zheda Institute for New Material and Chemical Enigeering (No. 2022SX-RF003).

Notes and references

1 L. Chouhan, S. Ghimire, C. Subrahmanyam, T. Miyasaka and V. Biju, Synthesis, Optoelectronic Properties and Applications of Halide Perovskites, *Chem. Soc. Rev.*, 2020, **49**, 2869–2885.
2 M. Z. Li and Z. G. Xia, Recent Progress of Zero-Dimensional Luminescent Metal Halides, *Chem. Soc. Rev.*, 2020, **50**, 2626–2662.
3 L. Zhou, J. F. Liao and D. B. Kuang, An Overview for Zero-Dimensional Broadband Emissive Metal-Halide Single Crystals, *Adv. Opt. Mater.*, 2021, **9**, 2100544.
4 L. N. Quan, F. P. García de Arquer, R. P. Sabatini and E. H. Sargent, Perovskites for Light Emission, *Adv. Mater.*, 2018, **30**, 1801996.
5 J. H. Wei, W. T. Ou, J. B. Luo and D. B. Kuang, Zero-Dimensional Zn-Based Halides with Ultra-Long Room-Temperature Phosphorescence for Time-Resolved Anti-Counterfeiting, *Angew. Chem., Int. Ed.*, 2022, **61**, e202207985.
6 T. Chen, Y. J. Ma and D. Yan, Single-Component 0D Metal-Organic Halides with Color-Variable Long-Afterglow toward Multi-Level Information Security and White-Light LED, *Adv. Funct. Mater.*, 2023, **33**, 2214962.
7 X. Wang, T. Bai, J. Sun, J. Liu, Y. Su and J. Chen, The Effect of Solvent on the Formation of Low-Dimensional Metal Halides and Their Self-Trapped Exciton Emission, *Chem. Eng. J.*, 2024, **486**, 150257.
8 Z. Luo, Y. Liu, Y. Liu, C. Li, Y. Li, Q. Li, Y. Wei, L. Zhang, B. Xu, X. Chang and Z. Quan, Integrated Afterglow and Self-Trapped Exciton Emissions in Hybrid Metal Halides for Anti-Counterfeiting Applications, *Adv. Mater.*, 2022, **34**, 2200607.
9 J. Han, Y. Li, P. Shen, Q. Li, Y. Liu, Y. Wei, P. Zhang and Z. Quan, Pressure-Induced Free Exciton Emission in a Quasi-Zero-Dimensional Hybrid Lead Halide, *Angew. Chem., Int. Ed.*, 2023, **63**, e202316348.
10 R. Gautier, M. Paris and F. Massuyeau, Exciton Self-Trapping in Hybrid Lead Halides: Role of Halogen, *J. Am. Chem. Soc.*, 2019, **141**, 12619–12623.
11 G. Zhou, X. Jiang, M. Molokeev, Z. Lin, J. Zhao, J. Wang and Z. Xia, Optically Modulated Ultra-Broad-Band Warm White Emission in Mn^{2+}-Doped $(C_6H_{18}N_2O_2)PbBr_4$ Hybrid Metal Halide Phosphor, *Chem. Mater.*, 2019, **31**, 5788–5795.
12 Z. Yuan, C. K. Zhou, Y. Tian, Y. Shu, J. Messier, J. C. Wang, L. J. van de Burgt, K. Kountouriotis, Y. Xin, E. Holt, K. Schanze, R. Clark, T. Siegrist and B. W. Ma, One-Dimensional Organic Lead Halide Perovskites with Efficient Bluish White-Light Emission, *Nat. Commun.*, 2017, **8**, 14051.
13 L. Zhou, J. F. Liao, Z. G. Huang, J. H. Wei, X. D. Wang, H. Y. Chen and D. B. Kuang, Intrinsic Self-Trapped Emission in 0D Lead-Free $(C_4H_{14}N_2)_2In_2Br_{10}$ Single Crystal, *Angew Chem. Int. Ed. Engl.*, 2019, **58**, 15435–15440.
14 M. D. Smith and H. I. Karunadasa, White-Light Emission from Layered Halide Perovskites, *Acc. Chem. Res.*, 2018, **51**, 619–627.
15 H. Chen, H. Xiang, Y. Zou, S. Zhang, B. Cai, J. Zhang, L. Hou and H. Zeng, Perspective on Metal Halides with Self-Trapped Exciton toward White Light-Emitting Diodes, *Adv. Opt. Mater.*, 2022, **10**, 2101900.
16 L. J. Xu, C. Z. Sun, H. Xiao, Y. Wu and Z. N. Chen, Green-Light-Emitting Diodes Based on Tetrabromide Manganese(II) Complex through Solution Process, *Adv. Mater.*, 2017, **29**, 1605739.
17 S. Yan, W. Tian, H. Chen, K. Tang, T. Lin, G. Zhong, L. Qiu, X. Pan and W. Wang, Synthesis of 0D Manganese-Based Organic-Inorganic Hybrid Perovskite and Its Application in Lead-Free Red Light-Emitting Diode, *Adv. Funct. Mater.*, 2021, **31**, 2100855.
18 G. Liu, M. S. Molokeev and Z. Xia, Structural Rigidity Control toward Cr^{3+}-Based Broadband Near-Infrared Luminescence with Enhanced Thermal Stability, *Chem. Mater.*, 2022, **34**, 1376–1384.
19 C. Shi, L. Ye, Z.-X. Gong, J.-J. Ma, Q.-W. Wang, J.-Y. Jiang, M.-M. Hua, C.-F. Wang, H. Yu, Y. Zhang and H.-Y. Ye, Two-Dimensional Organic-Inorganic Hybrid Rare-Earth Double Perovskite Ferroelectrics, *J. Am. Chem. Soc.*, 2020, **142**, 545–551.
20 G. Song, Z. Li, P. Gong, R. J. Xie and Z. Lin, Tunable White Light Emission in a Zero-Dimensional Organic-Inorganic Metal Halide Hybrid with Ultra-High Color Rendering Index, *Adv. Opt. Mater.*, 2021, **9**, 2002246.
21 S. Krishnamurthy, R. Naphade, W. J. Mir, S. Gosavi, S. Chakraborty, R. Vaidhyanathan and S. Ogale, Molecular and Self-Trapped Excitonic Contributions to the Broadband Luminescence in Diamine-Based Low-Dimensional Hybrid Perovskite Systems, *Adv. Opt. Mater.*, 2018, **6**, 1800751.
22 Z. Li, G. Song, Y. Li, L. Wang, T. Zhou, Z. Lin and R.-J. Xie, Realizing Tunable White Light Emission in Lead-Free Indium(III) Bromine Hybrid Single Crystals through Antimony(III) Cation Doping, *J. Phys. Chem. Lett.*, 2020, **11**, 10164–10172.
23 S. You, T. Zhu, Y. Wang, Z. K. Zhu, Z. Li, J. Wu, P. Yu, L. Li, C. Ji, Y. Wang, S. Wang and J. Luo, Exploring a Stable and Dense 3D Lead Chloride Hybrid with Emission of Self-

Trapped Excitons toward X-Ray Scintillation, *Adv. Funct. Mater.*, 2022, 2210481.

24 L. Lian, P. Zhang, X. Zhang, Q. Ye, W. Qi, L. Zhao, J. Gao, D. Zhang and J. Zhang, Realizing Near-Unity Quantum Efficiency of Zero-Dimensional Antimony Halides through Metal Halide Structural Modulation, *ACS Appl. Mater. Interfaces*, 2021, **13**, 58908–58915.

25 D. Han, H. Shi, W. Ming, C. Zhou, B. Ma, B. Saparov, Y.-Z. Ma, S. Chen and M.-H. Du, Unraveling Luminescence Mechanisms in Zero-Dimensional Halide Perovskites, *J. Mater. Chem. C*, 2018, **6**, 6398–6405.

26 Z. Qi, H. Gao, X. Zhu, Z. Lu and X. M. Zhang, Blue Light-Excitable Broadband Yellow Emission in a Zero-Dimensional Hybrid Bismuth Halide with Type-II Band Alignment, *Inorg. Chem.*, 2022, **61**, 19483–19491.

27 J.-C. Jin, Y.-P. Lin, D.-Y. Chen, B.-Y. Lin, T.-H. Zhuang, W. Ma, L.-K. Gong, K.-Z. Du, J. Jiang and X.-Y. Huang, X-Ray Scintillation and Photoluminescence of Isomorphic Ionic Bismuth Halides with $[Amim]^+$ or $[Ammim]^+$ Cations, *Inorg. Chem. Front.*, 2021, **8**, 4474–4481.

28 J. K. Pious, C. Muthu and C. Vijayakumar, Organic Spacer Cation Assisted Modulation of the Structure and Properties of Bismuth Halide Perovskites, *Acc. Chem. Res.*, 2022, **55**, 275–285.

29 H. Fattal, T. D. Creason, C. J. Delzer, A. Yangui, J. P. Hayward, B. J. Ross, M.-H. Du, D. T. Glatzhofer and B. Saparov, Zero-Dimensional Hybrid Organic-Inorganic Indium Bromide with Blue Emission, *Inorg. Chem.*, 2021, **60**, 1045–1054.

30 M. Chaaban, A. Ben-Akacha, M. Worku, S. Lee, J. Neu, X. Lin, J. S. R. Vellore Winfred, C. J. Delzer, J. P. Hayward, M. H. Du, T. Siegrist and B. Ma, Metal Halide Scaffolded Assemblies of Organic Molecules with Enhanced Emission and Room Temperature Phosphorescence, *J. Phys. Chem. Lett.*, 2021, **12**, 8229–8236.

31 J. Q. Zhao, M. F. Han, X. J. Zhao, Y. Y. Ma, C. Q. Jing, H. M. Pan, D. Y. Li, C. Y. Yue and X. W. Lei, Structural Dimensionality Modulation toward Enhanced Photoluminescence Efficiencies of Hybrid Lead-Free Antimony Halides, *Adv. Opt. Mater.*, 2021, **9**, 2100556.

32 L.-K. Wu, R.-F. Li, W.-Y. Wen, Q.-H. Zou, H.-Y. Ye and J.-R. Li, Lead-Free Hybrid Indium Perovskites with Near-Unity PLQY and White Light Emission Using an Sb^{3+} Doping Strategy, *Inorg. Chem. Front.*, 2023, **10**, 3297–3306.

33 C. Deng, S. Hao, K. Liu, M. S. Molokeev, C. Wolverton, L. Fan, G. Zhou, D. Chen, J. Zhao and Q. Liu, Broadband Light Emitting Zero-Dimensional Antimony and Bismuth-Based Hybrid Halides with Diverse Structures, *J. Mater. Chem. C*, 2021, **9**, 15942–15948.

34 S. Guo, Y. Li, Y. Mao, W. Tao, K. Bu, T. Fu, C. Zhao, H. Luo, Q. Hu, H. Zhu, E. Shi, W. Yang, L. Dou and X. Lü, Reconfiguring Band-Edge States and Charge Distribution of Organic Semiconductor-Incorporated 2D Perovskites *via* Pressure Gating, *Sci. Adv.*, 2022, **8**, eadd1984.

35 X. Li, X. Gao, X. Zhang, X. Shen, M. Lu, J. Wu, Z. Shi, V. L. Colvin, J. Hu, X. Bai, W. W. Yu and Y. Zhang, Lead-Free Halide Perovskites for Light Emission: Recent Advances and Perspectives, *Adv. Sci.*, 2021, **8**, 2003334.

36 H.-T. Sun, J. Zhou and J. Qiu, Recent Advances in Bismuth Activated Photonic Materials, *Prog. Mater. Sci.*, 2014, **64**, 1–72.

37 Y. Jing, Y. Liu, M. Li and Z. Xia, Photoluminescence of Singlet/Triplet Self-Trapped Excitons in Sb^{3+}-Based Metal Halides, *Adv. Opt. Mater.*, 2021, **9**, 2002213–2002227.

38 X. Liu, X. Xu, B. Li, Y. Liang, Q. Li, H. Jiang and D. Xu, Antimony-Doping Induced Highly Efficient Warm-White Emission in Indium-Based Zero-Dimensional Perovskites, *CCS Chem.*, 2020, **2**, 216–224.

39 J. Yuan, G. Zhou, J. Zhang and X.-M. Zhang, A Synergetic Model for Implementing Single-Component White-Light Emission: A Case Study of Zero-Dimensional Cadmium Halides, *Mater. Chem. Front.*, 2023, **7**, 705–712.

40 C. Sun, J.-P. Zang, Y.-Q. Liu, Q.-Q. Zhong, X.-X. Xing, J.-P. Li, C.-Y. Yue and X.-W. Lei, Lead-Free Hybrid Indium Perovskites with Highly Efficient and Stable Green Light Emissions, *CCS Chem.*, 2022, **4**, 3106–3121.

41 M. E. Sun, Y. Li, X. Y. Dong and S. Q. Zang, Thermoinduced Structural-Transformation and Thermochromic Luminescence in Organic Manganese Chloride Crystals, *Chem. Sci.*, 2019, **10**, 3836–3839.

42 J. Almutlaq, W. J. Mir, L. Gutiérrez-Arzaluz, J. Yin, S. Vasylevskyi, P. Maity, J. k. Liu, R. Naphade, O. F. Mohammed and O. M. Bakr, $CsMnBr_3$: Lead-Free Nanocrystals with High Photoluminescence Quantum Yield and Picosecond Radiative Lifetime, *ACS Mater. Lett.*, 2021, **3**, 290–297.

43 P. R. Spackman, M. J. Turner, J. J. McKinnon, S. K. Wolff, D. J. Grimwood, D. Jayatilaka and M. A. Spackman, CrystalExplorer: A Program for Hirshfeld Surface Analysis, Visualization and Quantitative Analysis of Molecular Crystals, *J. Appl. Crystallogr.*, 2021, **54**, 1006–1011.

44 M. A. Spackman and D. Jayatilaka, Hirshfeld Surface Analysis, *CrystEngComm*, 2009, **11**, 19–32.

45 G. Kresse and J. Furthmüller, Efficient Iterative Schemes for *Ab Initio* Total-Energy Calculations Using a Plane-Wave Basis Set, *Phys. Rev. B: Condens. Matter Mater. Phys.*, 1996, **54**, 11169–11186.

46 G. Kresse and D. Joubert, From Ultrasoft Pseudopotentials to the Projector Augmented-Wave Method, *Phys. Rev. B: Condens. Matter Mater. Phys.*, 1999, **59**, 1758–1775.

47 J. Heyd, G. E. Scuseria and M. Ernzerhof, Hybrid Functionals Based on a Screened Coulomb Potential, *J. Chem. Phys.*, 2003, **118**, 8207–8215.

48 T.-T. Liu, S.-Y. Tang, B. Hu, P. Liu, S. Bi and Y.-Y. Jiang, Mechanism and Origin of Chemoselectivity of Ru-Catalyzed Cross-Coupling of Secondary Alcohols to β-Disubstituted Ketones, *J. Org. Chem.*, 2020, **85**, 12444–12455.

49 J. A. Duffy, Trends in Energy Gaps of Binary Compounds: An Approach Based upon Electron Transfer Parameters from Optical Spectroscopy, *J. Phys. C: Solid State Phys.*, 1980, **13**, 2979–2989.

50 A. L. Allred, Electronegativity Values from Thermochemical Data, *J. Inorg. Nucl. Chem.*, 1961, **17**, 215–227.

51 T. Chang, Y. Dai, Q. Wei, X. Xu, S. Cao, B. Zou, Q. Zhang and R. Zeng, Temperature-Dependent Reversible Optical Properties of Mn-Based Organic-Inorganic Hybrid $(C_8H_{20}N)_2MnCl_4$ Metal Halides, *ACS Appl. Mater. Interfaces*, 2023, **15**, 5487–5494.

52 L. J. Xu, A. Plaviak, X. Lin, M. Worku, Q. He, M. Chaaban, B. J. Kim and B. Ma, Metal Halide Regulated Photophysical Tuning of Zero-Dimensional Organic Metal Halide Hybrids: From Efficient Phosphorescence to Ultralong Afterglow, *Angew. Chem., Int. Ed.*, 2020, **59**, 23067–23071.

53 B. Wu, W. Ning, Q. Xu, M. Manjappa, M. Feng, S. Ye, J. Fu, S. Lie, T. Yin, F. Wang, T. W. Goh, P. C. Harikesh, Y. K. E. Tay, Z. X. Shen, F. Huang, R. Singh, G. Zhou, F. Gao and T. C. Sum, Strong Self-Trapping by Deformation Potential Limits Photovoltaic Performance in Bismuth Double Perovskite, *Sci. Adv.*, 2021, **7**, eabd3160.

54 M. Bujak and R. J. Angel, Low-Temperature Single Crystal X-Ray Diffraction and High-Pressure Raman Studies on $[(CH_3)_2NH_2]_2[SbCl_5]$, *J. Solid State Chem.*, 2007, **180**, 3026–3034.

55 Z. Wang, D. Xie, F. Zhang, J. Yu, X. Chen and C. P. Wong, Controlling Information Duration on Rewritable Luminescent Paper Based on Hybrid Antimony (III) Chloride/Small-Molecule Absorbates, *Sci. Adv.*, 2020, **6**, eabc2181.

56 Q. Wei, T. Chang, R. Zeng, S. Cao, J. Zhao, X. Han, L. Wang and B. Zou, Self-Trapped Exciton Emission in a Zero-Dimensional $(TMA)_2SbCl_5 \cdot DMF$ Single Crystal and Molecular Dynamics Simulation of Structural Stability, *J. Phys. Chem. Lett.*, 2021, **12**, 7091–7099.

57 J. Yuan, Z. Qi, J. Zhang, N. Zhang and X. M. Zhang, Improving Photoelectron Localization to Significantly Enhanced Broadband Orange-Light Emission in Hybrid Antimony Halides with Sb–Cl Secondary Bonding, *Laser Photonics Rev.*, 2024, 2301264.

58 D.-Y. Li, Y. Cheng, Y.-H. Hou, J.-H. Song, C.-J. Sun, C.-Y. Yue, Z.-H. Jing and X.-W. Lei, Modulating Photoelectron Localization Degree to Achieve Controllable Photoluminescence Quenching and Activation of 0D Hybrid Antimony Perovskites, *J. Mater. Chem. C*, 2022, **10**, 3746–3755.

59 K. Han, J. Qiao, S. Zhang, B. Su, B. Lou, C. G. Ma and Z. Xia, Band Alignment Engineering in ns^2 Electrons Doped Metal Halide Perovskites, *Laser Photonics Rev.*, 2022, **17**, 2200458.